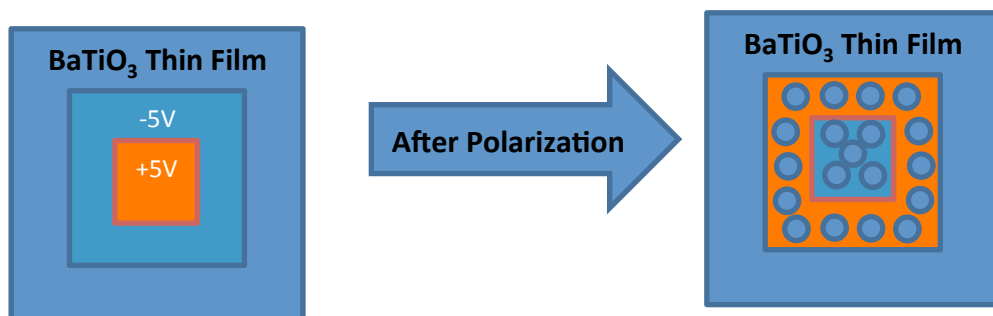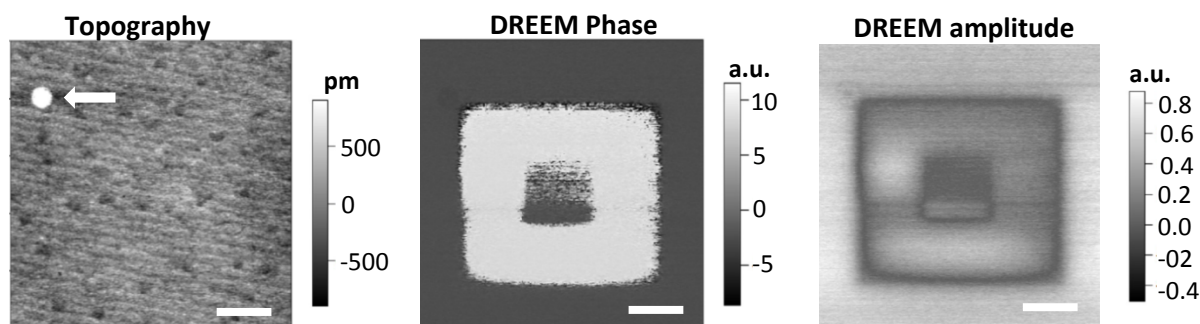**A**

B

Figure S1, related to Figure 1. Topographic and DREEM images of a polarized BaTiO₃ (BTO) thin film. (A) Schematic showing the generation of a surface pattern with different polarization states on a BTO film. External electric fields (-5V DC bias for the larger area followed by +5V bias for the smaller area) are applied through a conductive AFM cantilever. The charge density on the BTO thin film after polarization was estimated to be approximately 2 electrons/nm². (B) Topographic (left), DREEM phase (middle), and DREEM amplitude (right) images of the polarized areas on the BTO thin film. The DREEM phase and amplitude images directly reveal the pattern of charged areas, without any detectable crosstalk into the topographic channel. In addition, the large contaminant particle seen in the topographic image (white arrow) is not seen in the DREEM images, indicating that there is no crosstalk of the topographic signal into the DREEM signals. The XY scale bars are 1 μm.
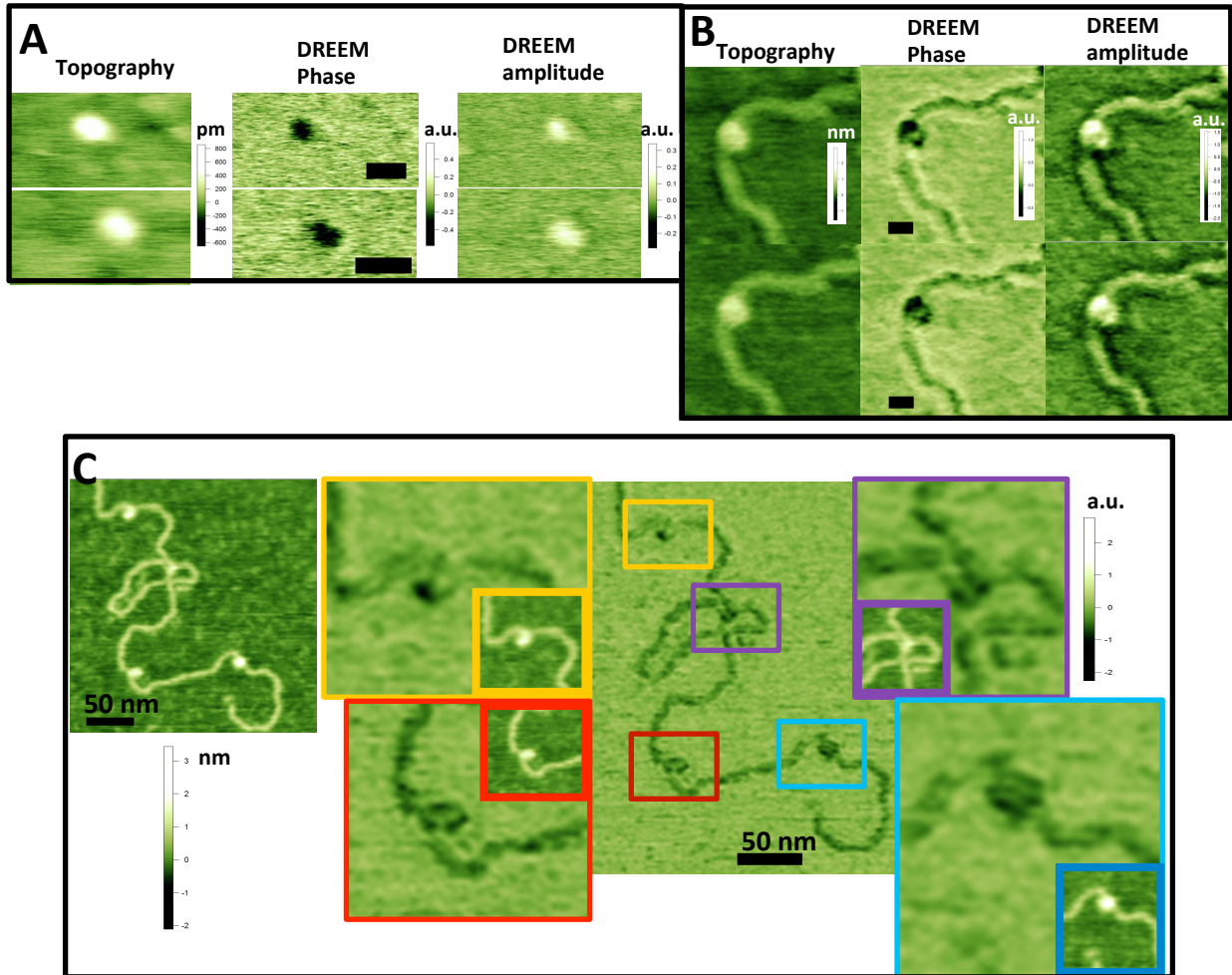
Figure S2, related to Figure 2. Additional DREEM Images of histone alone and nucleosomes. (A) DREEM images of histone proteins alone in the absence of DNA. Topographic (*left panels*), DREEM phase (*middle panels*), and DREEM amplitude (*right panels*) images of two individual histone proteins (top and bottom panels). (B) Repeated scans (*top panels*) and retrace images (*bottom panels*) of the nucleosome shown in Figure 2B. The topographic (*left panels*), DREEM phase (*middle panels*), and DREEM amplitude images (*right panels)* demonstrate the reproducibility of DREEM imaging. The XY scale bars are 20 nm. (C) DREEM imaging reveals DNA paths on multiple nucleosomes in individual images. *Left panel:* The topographic image. *Right panel*: A DREEM phase image of the same DNA molecule with multiple nucleosomes (*middle image*). Zoomed in areas with individual nucleosomes are shown surrounding the full image. Each nucleosome is identified by the matching color outlining the nucleosome molecules in the middle image. The inserts in the zoomed-in images show the corresponding topographic images (not to scale). The DNA paths revealed in DREEM images are at different orientations, ruling out the possibility that the signals consistent with DNA paths are due to scanning artefacts.
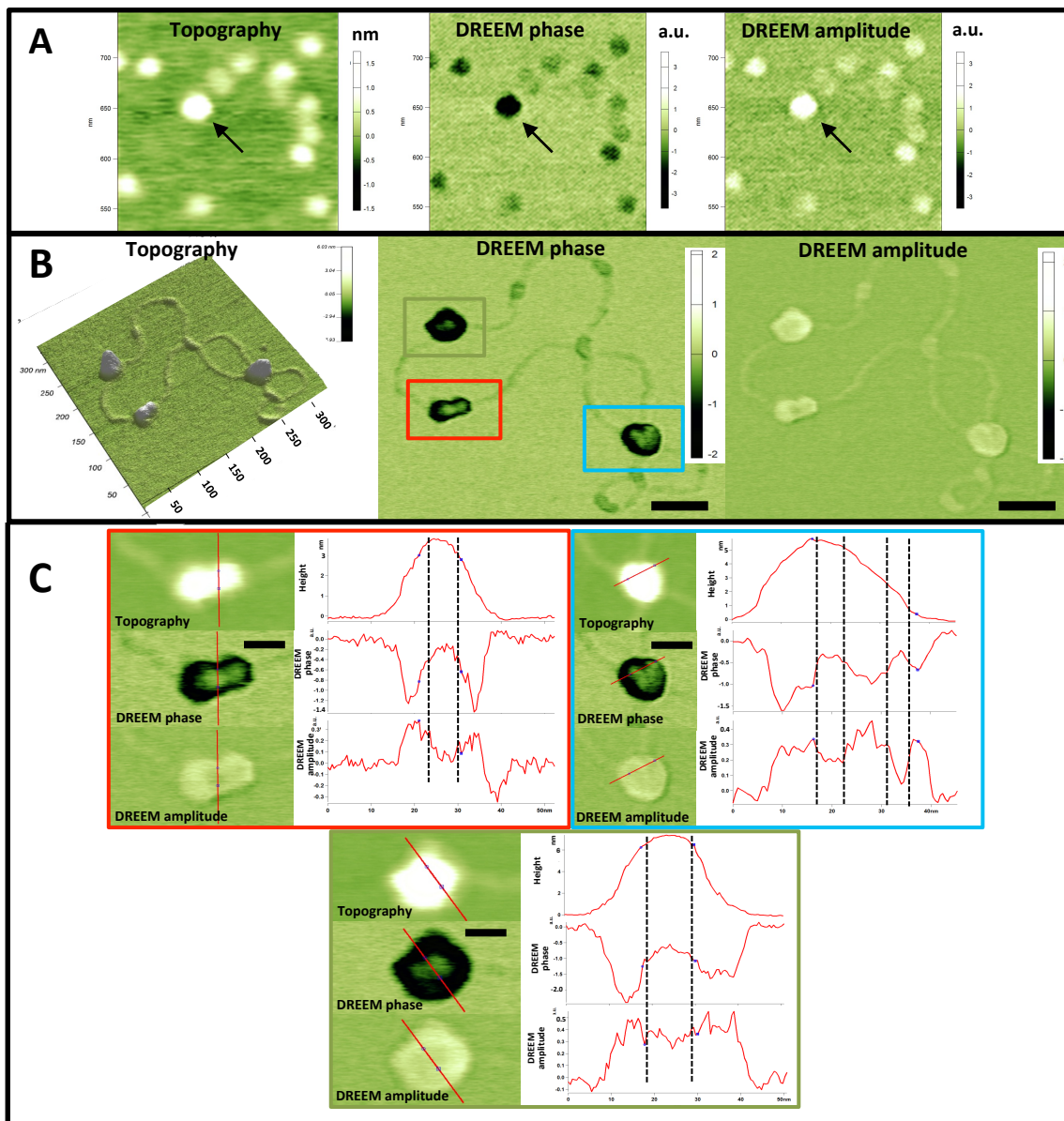
Figure S3, related to Figure 3. DREEM imaging reveals the path of the DNA in hMutSα mobile clamp complexes loaded onto a circular DNA substrate (4 kbp) containing two GT mismatches 2 kbp apart. (A) Topographic (*left*), DREEM phase (*middle*), and DREEM amplitude (*right*) images of a sample containing both hMutLα, which adopts multiple conformations (Sacho *et al*. *Mol Cell* 2008, 29:112-21), and hMutSα without DNA (hMutSα MW=257 kDa; hMutLα MW=180 kDa). The larger protein is hMutSα (identified by arrow). (B) Topographic (left), DREEM phase (middle), and DREEM amplitude (right) of multiple hMutSα sliding clamps formed by incubating 125 nM hMutSα and 1 mM ATP with the mismatch containing DNA. Based on the volume of the complexes in the topographic images, each of the complexes (in boxed regions) contain two or more hMutSα proteins. The scale bars are 50 nm. (C) Zoomed-in images showing the cross-section analysis of the hMutSα-DNA complexes in the boxed regions in B. The scale bars are 20 nm. The pairs of perpendicular lines on the section plots indicate the positions of the DNA strands. In the zoomed-in image in C (top left) (as well as in the overview image in B) two MutSα proteins can clearly be seen adjacent to one another on the DNA. In C (top right), the MutSα complex is interacting with two DNA stands, and the two individual duplex DNA strands can be clearly seen in the DREEM images and the cross-section analysis. Only DREEM images, but not topographic images reveal the DNA in hMutSα-DNA complexes.

Supplemental Information

Theoretical basis of DREEM measurements

As demonstrated below, because we are monitoring very small changes in surface potential on a modestly charged surface (mica), $\Delta A_{\omega_2}(x,y)$ will be dominated by changes in the force gradient, with only small contributions from the force. This method is similar to amplitude slope detection method used to monitor the atomic force gradient in topographic AFM images (Martin et al., 1987).

Because the AC bias is applied at the first overtone frequency (ω_2), the applied force induces a vibration, with a free amplitude (assuming no dampening)

$$A_{0,\omega_2} = \left(Q_2/k_2\right)F_{\omega_2} = a\left(Q_2/k_2\right)\frac{\partial C}{\partial z}(\Delta\phi_{TS} - V_{DC})V_{AC} \,,$$

where Q_2 and k_2 are the quality factor and effective spring constant, respectively, of the first overtone of the cantilever, and a is a constant that depends on the tip radius, and tip-sample separation (García and Perez, 2002; Nonnenmacher et al., 1991; Rast et al., 2000). In addition, the force gradient, F', changes the effective spring constant of the cantilever and shifts its first overtone frequencies by

$$\Delta\omega_2 = \omega_2 F'/2k_c$$

where k_c is the spring constant of the cantilever (which is equal to k_1, the spring constant of ω_1) (Albrecht et al., 1991; Hoummady and Farnault, 1998; Martin et al., 1987), thereby reducing the vibration amplitude at ω_2 to

$$A_{\omega_2} \approx A_{0,\omega_2}\left[1 + b\left(Q_2/k_c\right)F'\right]$$

This approximation assumes that the applied force is slightly off the resonance frequency on the side of the resonance peak, where the slope of the peak is maximum and $b = \dfrac{2}{3\sqrt{3}}$ (Martin et al., 1987). Notably, the frequency shift and therefore the change in amplitude depend on both the static and dynamic components of the electrostatic force gradient (*i.e.*, F'_{DC} and F'_{ω_2}; eq. 1 & 2) (García and Perez, 2002; Takagi et al., 2009).

Because we are operating in intermittent contact, the force gradient (F'_a) due to repulsive atomic interactions is significantly greater than that due to the attractive electrostatic interactions (F'_{el}) (Hong et al., 1998; Hong et al., 1999); therefore, $\Delta\omega_2 > 0$. (We verified that $\Delta\omega_2 > 0$ in our experiments by monitoring the vibration amplitude as a function of the AC bias frequency.) Under our imaging conditions, A_{ω_2} is ~1/2 A_{0,ω_2} after engaging in repulsive mode. During scanning, however, F'_a should be constant because the topographic signal at ω_1 maintains a constant atomic force gradient, and therefore, changes in $\Delta\omega_2(x,y)$ will be dominated by F'_{el}. In addition, because $F'_a \gg F'_{DC}$, F'_{DC} does not significantly contribute to the signal at ω_1. Consequently, the static electrical force gradient does not affect the topographic image, and therefore, F'_{DC} is not maintained constant during imaging and will contribute to the signal at ω_2. We confirmed that F'_{DC} does not affect the topographic images by turning the modulated bias voltage on and off while scanning.

Assuming that the atomic force gradient is constant as a function of x,y position of the tip, the change in A_{ω_2} ($\Delta A_{\omega_2}(x,y)$) due to changes in the electrostatic force and force gradient associated with a change in position from (x_1,y_1) to (x_2,y_2) on the surface is approximately

$$\Delta A_{\omega_2}(x,y) \approx \left(\frac{Q_2}{k_2}\right)\left[\Delta F_{\omega_2,el}(x,y) + b\left(\frac{Q_2}{k_c}\right)\Delta(F_{\omega_2,el}(x,y)F'_{el}(x,y))\right]$$

$$\Delta A_{\omega_2}(x,y) \approx \left(\frac{Q_2}{k_2}\right)\left(\Delta F_{\omega_2,el}(x,y) + b\left(\frac{Q_2}{k_c}\right)\left\{\left[F_{\omega_2,el}(x_1,y_1) + \Delta F_{\omega_2,el}(x,y)\right]F'_{el}(x_2,y_2) - F_{\omega_2,el}(x_1,y_1)F'_{el}(x_1,y_1)\right\}\right)$$

For small changes in surface potential [$\Delta\psi(x,y)$] or capacitance, such as those in the current experiments where $\Delta\psi(x,y)$ and capacitance changes are very small (only the difference in potential and/or capacitance between the mica substrate and the deposited protein and DNA molecules), $\Delta F_{\omega_2,el}(x,y) << F_{\omega_2,el}$ and

$$\Delta A_{\omega_2}(x,y) \approx \left(\frac{Q_2}{k_2}\right)\left(\Delta F_{\omega_2,el}(x,y) + b\left(\frac{Q_2}{k_c}\right)F_{\omega_2,el}\Delta F'_{el}(x,y)\right)$$

Because $F_{\omega_2,el}$ is sensitive to electrostatic potential over a greater distance than F'_{el}, the tip cone and the cantilever, as well as the tip apex, make contributions to $F_{\omega_2,el}(x,y)$, and therefore, $F_{\omega_2,el}(x,y)$ will be averaged over a greater area of the sample than $F'_{el}(x,y)$ (Colchero et al., 2001; Ding et al., 2009; Giessibl, 1995; Gil et al., 2003; Glatzel, 2003; Martin et al., 1987; Tevaarwerk et al., 2005). Consequently, for small changes in capacitance and surface potential [*i.e.*, $\Delta\psi(x,y) << (\Delta\phi_{TS}-V_{DC})$] over an area similar to the tip radius, $F_{\omega_2,el}(x,y)$ may be relatively constant. If the force is approximately constant as a function of position then

$$\Delta A_{\omega_2}(x,y) \approx b\left(\frac{Q_2^2}{k_c k_2}\right)F_{\omega_2,el}\Delta F'_{el}(x,y)$$

and only the force gradient contributes to $\Delta A_{\omega_2}(x,y)$. (For the cantilevers used in our experimental setup, $k_c \approx 2.8$ N/m, $k_2 \approx 110$ N/m, $Q_1 \approx 170$, and $Q_2 \approx 500$.). Because $\Delta\psi << (\Delta\phi_{TS}-V_{DC})$ for proteins and DNA deposited on mica (Leung et al., 2009; Leung et al., 2010), $\Delta A_{\omega_2}(x,y)$ is dominated by F'_{el}.

Supplemental Experimental Procedures

Conductive cantilever preparation

To obtain high-resolution topography and DREEM images, we used highly doped silicon

cantilevers (PPP-FMR from Nanosensor; 2.8 N/m) instead of metal coated cantilevers, because

the radius of curvature of the metal coated tip is ~ 20 nm, while that for the non-coated tip is ~ 7

nm. The conductivity of the doped cantilevers is comparable to that of the metal coated tips. It

should be noted, however, that these doped silicon tips are easily oxidized, which results in the

formation of a nanometer thin non-conductive oxidized layer. Consequently, to make a

conductive connection between the cantilever and the external input power source, it is essential

to penetrate the oxide layer. As described below, we have devised a straightforward method for

making a reliable connection, by scraping the cantilever chip and simultaneously coating it with

colloidal liquid silver. The silver on the chip makes contact with the metallic tip holder for the

Asylum AFM system. For use with instruments that do not have grounded tip holders, ground

wires can be attached with patch of liquid silver.

   Detailed instructions for cantilever preparation. A small amount of the colloidal liquid

silver (Ted Pella Inc. product #16034) is spread on a clean glass slide. The cantilever is held with

one pair of tweezers. Another pair of tweezers is dipped in the liquid silver, and these silver

coated tweezers are used to scrape and coat the edges of the silicon chip and the silicon surface

of the chip on the side opposite from the cantilever tip. The scraping removes the oxidized

silicon (SiO_2) layer on the surface and replaces it with a conductive silver layer. This process

simultaneously scratches away the oxide layer and covers the silicon with silver, preventing any

oxidation and forming a conductive layer that can be easily connected to the external electrical

sources. Once the coating is completed, the silver coated chip is allowed to dry for ~5 minutes,

and it then can be loaded into the AFM.

Substrate grounding

In our setup, the bias is applied to the tip and the sample is grounded. To ground the sample, which is deposited on mica, we use liquid silver to connect a thin piece of mica to a glass slide, and we also make a connection to ground using liquid silver. Specifically, after the sample has been deposited on mica, a box cutter is used to cleave a thin layer of mica containing the deposited samples (on the topside). The opposite side of the mica (the downside), which does not contain the sample, is coated with liquid silver and held in the air until the liquid silver is dried. This sample is then attached to a glass slide with liquid silver.

To prepare the glass slide, the center of a glass slide is coated with a patch of liquid silver at least as large as the mica. A streak of silver leading from this central patch to one of the furthest sides is painted, and the streak is continued for a short distance on the other side of the glass slide to ensure that it makes proper contact with the metal on the AFM base for grounding. The silver-coated mica is placed, silver side down, on the wet silver patch, and the slide is allowed to dry for ~30 minutes. It is important not to press down too hard when placing the mica on the silver patch to avoid causing patches where there is no silver.

Selection of the imaging conditions

AFM topographic images are collected in standard repulsive intermittent contact mode at the fundamental resonance frequency (ω_1) (MFP-3D AFM, Asylum Research). With the cantilevers used in this study (PPP-FMR from Nanosensor; 2.8 N/m), we found that the highest quality topographic images were obtained with a vibration amplitude of 30 to 50 nm and a set point such that the force on the sample is minimized, while maintaining a repulsive interaction with surface. Not surprisingly, we found that the quality of the DREEM images is highly dependent on the quality of the topographic images. To determine the optimum AC and DC biases for DREEM imaging, we measured A_{ω_2} and collected images as a function of V_{AC} and V_{DC}

(from 0 to 20 V and -2.5 to 2.5 V, respectively) using the instrumental setup shown in Figure 1. Images were collected on two different custom modified MFP-3D Asylum Research AFMs in two different labs (DAE and HW).

The DREEM images of the nucleosomal arrays were taken at V_{AC} ~ 20 V and V_{DC} between ±2.5 V, depending on the tip. The magnitude of the applied DC voltage was adjusted based on the resolution and contrast of the DREEM images to achieve the highest signal to noise ratios. When the tip is in contact with mica in either repulsive or attractive mode and tuned near the optimum DC voltage, A_{ω_2} increases linearly upon varying V_{AC} from 0 to 20V, as expected (Mikamo-Satoh et al., 2009). The time constant for collection of the DREEM signal at ω_2 is 1 ms. Images were collected at a scan speed of 2 Hz, and the scan speed is limited by collection of the topographic signal, not the DREEM signal. The largest amplitudes that we employed for DREEM imaging at the first overtone are very small (~ 1 nm) compared to the mechanical vibration (30 to 50 nm) at the fundamental frequency, which prevents crosstalk of the electrical signal into the topographic signal. As expected, we also did not detect any crosstalk from the topography in the DREEM images (Figure S1), and no distinct signals are observed without applied biases. Also, we found that the larger protein-DNA complexes gave a better contrast between the DNA and the proteins, as compared to the smaller ones, probably because the greater amount of protein provides higher contrast. Similar to conventional AFM imaging techniques, DREEM imaging also can also experience tip artifacts, which are primarily due to the asymmetry in the electric field between the cantilever and sample surface. For example, in some cases, half-moon like asymmetries, with one side of the signal consistently higher than the other side, are seen in the same orientation for all complexes and proteins in a single image. Such images are discarded and not included in analyses. As with artifacts in conventional AFM images, these artifacts can be identified by their repetitive nature and by scanning at various angles, speeds, and size ranges, and by rotating the sample. Similar to conventional AFM

imaging, preparing clean samples and conductive tips, and driving the tip at the minimum

possible drive amplitude minimize the artifacts.

Sample preparation, deposition and analysis

The BaTiO$_3$ (BTO) thin film was fabricated by atomic layer controlled growth with in-situ

monitoring using high pressure reflection high energy electron diffraction (RHEED) (Choi et al.,

2004; Eom et al., 1992). External electrical fields (DC bias) applied through a conductive AFM

cantilever during scanning were used to locally polarize the BTO thin film and to generate a

surface pattern with different polarization states.

Reconstitution of nucleosomes was done using a linear 2743 bp DNA substrate that was

generated through XbaI restriction digestion of plasmid containing 601 (pGEM-3z/601,

Addgene) nucleosomal positioning sequences (Lowary and Widom, 1998). The reconstitution

was done using histones (EpiCypher) and the salt dialysis method (Carruthers et al., 1999). In

some cases, the nucleosomes were crosslinked with gluteraldehyde (Sigma Aldrich) for 30 min

at room temperature. The crosslinked or uncrosslinked nucleosomal arrays were deposited on

the freshly prepared aminopropyl triethoxy silane (APTES)-treated mica surface and incubated

for 10-15 minutes before rinsing (Shlyakhtenko et al., 2003). *Taq* MutS, human MutSα and

MutLα were purified using the protocols published previously (Geng et al., 2012; Sass et al.,

2010). For MutS-DNA complexes, the proteins and DNA were incubated together at room

temperature for two minutes, crosslinked with 0.8% gluteraldehyde for 1 min. The DNA is a

linearized 2030 base pair plasmid containing a single GT-mismatch (375 base pairs from one

end) (Geng et al., 2012), which serves as a recognition site for MutS and hMutSα. Some protein-

DNA complexes were purified using an approximately two-centimeter agarose bead gel filtration

column prior to deposition to remove excess free proteins. The complexes were deposited on

APTES-treated mica (Shlyakhtenko et al., 2003), immediately rinsed with water, and dried with

nitrogen, before imaging. The mica was exposed to APTES for only 15 minutes so that the mica surface contains a low density of amine groups. The DNA lengths were measured using the Asylum Research Software. The volume analysis was done as described previously (Ratcliff and Erie, 2001; Yang et al., 2003).

Supplemental References

Albrecht, T.R., Grütter, P., Horne, D., and Rugar, D. (1991). Frequency modulation detection using high-Q cantilevers for enhanced force microscope sensitivity. J. Appl. Phys. *69*, 668-673.

Carruthers, L.M., Tse, C., Walker, K.P., 3rd, and Hansen, J.C. (1999). Assembly of defined nucleosomal and chromatin arrays from pure components. Methods Enzymol. *304*, 19-35.

Choi, K.J., Biegalski, M., Li, Y.L., Sharan, A., Schubert, J., Uecker, R., Reiche, P., Chen, Y.B., Pan, X.Q., Gopalan, V.*, et al.* (2004). Enhancement of ferroelectricity in strained BaTiO3 thin films. Science *306*, 1005-1009.

Colchero, J., Gil, A., and Baró, A. (2001). Resolution enhancement and improved data interpretation in electrostatic force microscopy. Physical Review B *64*.

Ding, X.D., An, J., Xu, J.B., Li, C., and Zeng, R.Y. (2009). Improving lateral resolution of electrostatic force microscopy by multifrequency method under ambient conditions. Appl. Phys. Lett. *94*, 223109.

Eom, C.B., Cava, R.J., Fleming, R.M., Phillips, J.M., Vandover, R.B., Marshall, J.H., Hsu, J.W., Krajewski, J.J., and Peck, W.F., Jr. (1992). Single-Crystal Epitaxial Thin Films of the Isotropic Metallic Oxides Sr1-xCaxRuO3 (0 le x le 1). Science *258*, 1766-1769.

García, R., and Perez, R. (2002). Dynamic atomic force microscopy methods. Surf. Sci. Rep.

Geng, H., Sakato, M., DeRocco, V., Yamane, K., Du, C., Erie, D.A., Hingorani, M., and Hsieh, P. (2012). Biochemical analysis of the human mismatch repair proteins hMutSalpha MSH2(G674A)-MSH6 and MSH2-MSH6(T1219D). The Journal of biological chemistry *287*, 9777-9791.

Giessibl, F.J. (1995). Atomic resolution of the silicon (111)-(7x7) surface by atomic force microscopy. Science *267*, 68-71.

Gil, A., Colchero, J., Gómez-Herrero, J., and Baró, A. (2003). Electrostatic force gradient signal: resolution enhancement in electrostatic force microscopy and improved Kelvin probe microscopy. Nanotechnology *14*, 332.

Glatzel, T. (2003). Amplitude or frequency modulation-detection in Kelvin probe force microscopy. Appl. Surf. Sci. *210*, 84-89.

Hong, J., Kahng, D., Shin, J., Kim, H., and Khim, Z. (1998). Detection and control of ferroelectric domains by an electrostatic force microscope. Journal of Vacuum Science & Technology B: Microelectronics and Nanometer Structures *16*, 2942.

Hong, J., Park, S., and Khim, Z. (1999). Measurement of hardness, surface potential, and charge distribution with dynamic contact mode electrostatic force microscope. Rev. Sci. Instrum. *70*, 1735.

Hoummady, M., and Farnault, E. (1998). Enhanced sensitivity to force gradients by using higher flexural modes of the atomic force microscope cantilever. Applied Physics A: Materials Science & Processing *66*, 361-364.

Leung, C., Kinns, H., Hoogenboom, B.W., Howorka, S., and Mesquida, P. (2009). Imaging surface charges of individual biomolecules. Nano Lett. *9*, 2769-2773.

Leung, C., Maradan, D., Kramer, A., Howorka, S., Mesquida, P., and Hoogenboom, B.W. (2010). Improved Kelvin probe force microscopy for imaging individual DNA molecules on insulating surfaces. Appl. Phys. Lett. *97*, 203703.

Lowary, P.T., and Widom, J. (1998). New DNA sequence rules for high affinity binding to histone octamer and sequence-directed nucleosome positioning. J. Mol. Biol. *276*, 19-42.

Martin, Y., Williams, C.C., and Wickramasinghe, H.K. (1987). Atomic force microscope–force mapping and profiling on a sub 100-Å scale. J. Appl. Phys. *61*, 4723-4729.

Mikamo-Satoh, E., Yamada, F., Takagi, A., Matsumoto, T., and Kawai, T. (2009). Electrostatic force microscopy: imaging DNA and protein polarizations one by one. Nanotechnology *20*, 145102.

Nonnenmacher, M., O'Boyle, M.P., and Wickramasinghe, H.K. (1991). Kelvin probe force microscopy. Appl. Phys. Lett. *58*, 2921.

Rast, S., Wattinger, C., Gysin, U., and Meyer, E. (2000). The noise of cantilevers. Nanotechnology *11*, 169.

Ratcliff, G.C., and Erie, D.A. (2001). A novel single-molecule study to determine protein--protein association constants. JACS *123*, 5632-5635.

Sass, L.E., Lanyi, C., Weninger, K., and Erie, D.A. (2010). Single-molecule FRET TACKLE reveals highly dynamic mismatched DNA-MutS complexes. Biochemistry *49*, 3174-3190.

Shlyakhtenko, L.S., Gall, A.A., Filonov, A., Cerovac, Z., Lushnikov, A., and Lyubchenko, Y.L. (2003). Silatrane-based surface chemistry for immobilization of DNA, protein-DNA complexes and other biological materials. Ultramicroscopy *97*, 279-287.

Takagi, A., Yamada, F., Matsumoto, T., and Kawai, T. (2009). Electrostatic force spectroscopy on insulating surfaces: the effect of capacitive interaction. Nanotechnology *20*, 365501.

Tevaarwerk, E., Keppel, D.G., Rugheimer, P., Lagally, M.G., and Eriksson, M.A. (2005). Quantitative analysis of electric force microscopy: The role of sample geometry. Rev. Sci. Instrum. *76*, 053707.

Yang, Y., Wang, H., and Erie, D.A. (2003). Quantitative characterization of biomolecular assemblies and interactions using atomic force microscopy. Methods *29*, 175-187.